Analysis of test beam data taken with a prototype of TPC with resistive Micromegas readout for T2K Near Detector upgrade

---

Abstract

In this paper we describe the performances of a prototype of the High Angle Time Projection Chambers (HA-TPCs) that are being produced for the Near Detector (ND280) upgrade of T2K. In their final design two HA-TPCs will be produced and instrumented with eight Resistive MicroMegas modules (ERAM) on each endplate. This innovative techniques induces a spreading of the charge over several pads, improving the determination of the track position.

The TPC prototype has been equipped with the first ERAM module produced for T2K and with the HA-TPC electronics chain and it has been exposed to the DESY Test Beam in order to measure spatial and dE/dx resolution. In addition, for the first time, we compare the observed performances with a newly developed simulation of the ERAM detectors.

Spatial resolution better than 800 μm and dE/dx resolution better than 9% are observed for all the incident angles and all the drift distances. All the main features of the data are correctly reproduced by the simulation and these performances fully fulfill the requirements for the HA-TPCs of T2K.

Keywords: Resistive Micromegas, T2K Near Detector Time Projection Chambers

---

Contents

Preprint submitted to Nuclear Instruments and Methods *October 7, 2022*

1. Introduction

T2K is a long-baseline neutrino oscillation experiment that is taking data in Japan since 2010 [1]. By using an intense muon neutrino beam produced at the J-PARC accelerator complex and searching for the appearance of electron neutrinos at the far detector, Super-Kamiokande, T2K provided the first indications of θ_{13} different from zero [1] followed by the first measurement of neutrino oscillations in appearance mode [2]. Recently first hints of Charge-Parity (CP) violation in the leptonic sector were also published by T2K [3].

In order to confirm these hints, T2K is now preparing the second phase of the experiment, that includes an upgrade of the neutrino beamline and of the off-axis Near Detector complex, ND280.

ND280 is a magnetized multi-purpose detector with several sub-detectors installed inside the UA1 magnet that provide a magnetic field of 0.2 T. The core of ND280 is a tracker system, composed by two Fine Grained Detectors (FGDs) and three Time Projection Chambers (TPCs) instrumented with Bulk Micromegas modules. The TPCs are used to track charged particles emitted in neutrino interactions and measure their charge and momentum and perform particle identification based on the ionization in the gas. ND280 has been extensively used in all T2K oscillation analyses and allow to reduce systematic uncertainties to the 4–5% level.

To further reduce these uncertainties, the ND280 upgrade consists in replacing one of the ND280 sub-detectors, the P0D, with a new tracker system composed by a 3-dimensional scintillator target (Super-FGD), made of $\sim$2 millions of 1 cm^3 scintillator cubes each readout by three wavelength shifting fibers, two High Angle TPCs (HA-TPCs) and six Time-Of-Flight planes. Among other improvements, this upgrade, that will be installed in J-PARC in 2023, is expected to have better efficiency to reconstruct high angle and backward going tracks emitted in neutrino or antineutrino interactions thanks to the presence of the HA-TPCs.

Each endplate of the HA-TPC will be instrumented with 8 Encapsulated Resistive Anode Micromegas (ERAM). This technology, initially developed for the ILC prototypes [4], allows to spread the charge over several pads, improving the space point resolution. Different ERAM prototypes have been used for beam tests at CERN [5] and at DESY [6]. The results of these test beam allowed to validate the ERAM design and start the production of the 32 ERAMs that will be used to instrument the HA-TPCs.

One of these ERAM detectors was tested using an X-ray test bench at

CERN and then mounted in a prototype of the field cages that is being constructed for the HA-TPCs. This field cage prototype has the same construction materials, the same drift length ($\sim 1\ m$) and the same configuration for the electric field as the cages that are being constructed for the ND280 Upgrade. Also the full electronic chain that will be used for the HA-TPCs, including two Front-End-Cards (FEC) each hosting eight AFTER chips [7], one Front-End-Mezzanine (FEM) and the Back-End electronics (TDCM) was mounted on the field cage.

The TPC was placed inside a 1T PCMAG solenoid and exposed to an electron beam with momenta between 1 and 4 GeV/c at the DESY T24/1 facility. As we will show in this paper, this test beam campaign allowed to validate the performances of the TPCs for tracks with different incident angles with respect to the ERAM detector and for all the drift distances of interest for the T2K TPCs. With respect to the results presented in [6], these results are compared with a simulation that has been developed by using the ND280 software, adding the HA-TPCs ERAM geometry and the features of the resistive layers and of the AFTER electronics response.

As we will show in the rest of this paper, the ERAM detector allows to reach an excellent spatial resolution, below 800 μm for all the incident angles and drift distances, and an excellent dE/dx resolution, below 9% for tracks crossing the entire ERAM module. These performances are in good agreement with the ones predicted by the simulation that is able to reproduce both, low level variables, such as the charge sharing between neighboring pads or their time difference, as well as the spatial and the dE/dx resolution.

2. Experimental setup

2.1. HA-TPC field cage prototype

One of the main innovations of the HA-TPCs with respect to the vertical TPCs used in ND280 is that the new field cage will use a single layer of solid insulator laminated on a composite material, while for the current ND280 TPCs, two gas-tight boxes, one inside the other were used. This design allows to minimize the dead space and maximize the tracking volume.

In order to test the construction process of the HA-TPCs field cages, several prototypes have been produced and the last one, that share all the characteristics of the final field cages was used for the test beam described in this paper.

The field cage prototype is built with lightweight and low-Z mechanical structures with an hollow shell shape constituting the box. The box is laminated on a Aluminum mold in several layers, namely Kapton sheets, aramide fiber-fabrics peels and honeycomb spacer panels glued together. The field cage is then enclosed on the two sides with a cathode plane and the anode where the ERAM detector is located.

The innermost cage wall surface embeds a double layer of thin Copper strips: the ”fields” strips for degrading the potential from the cathode to the anode and the ”mirror” strips, for regularizing the field nearby the walls and for mitigating the effects of free charge deposition on dielectric surfaces. The strip foils are produced by the CERN Micro-Pattern Technologies service. In order to protect the field cage from the possible presence of tiny carbon fibers embedded into the aramide fiber fabric (Twaron) the mirror strip side is protected with an additional Kapton coverlay glued on it.

The prototype has the same drift length (1 m) as the HA-TPCs and a reduced transverse scale (0.42 $m \times 0.42$ m) suitable to host one ERAM module. It was produced by the NEXUS company (Barcelona, Spain) and the different phases of the production of the prototype are shown in Fig. 1

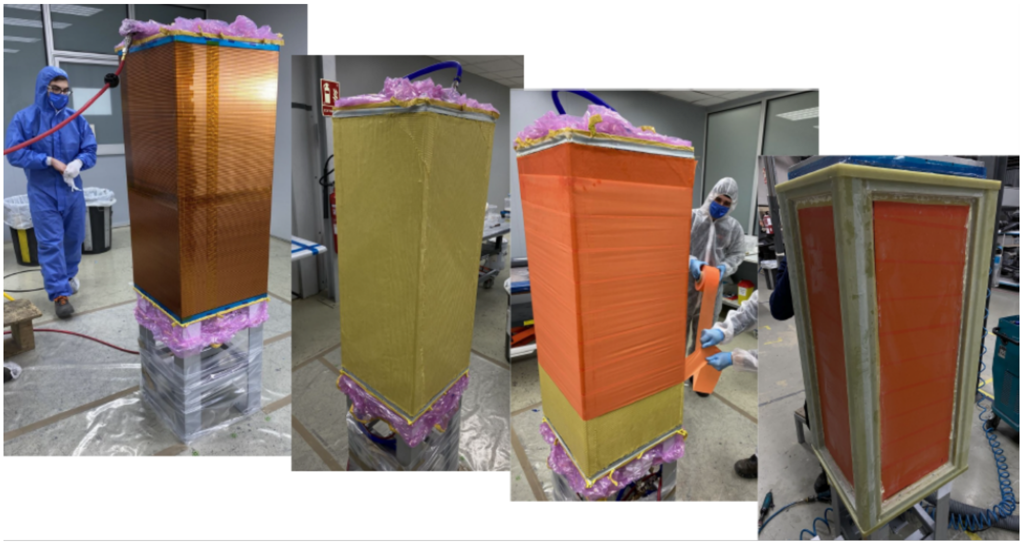

Figure 1: Phases of a prototype production. from left to right: strip foil wrapped onto the mold, aramid fiber fabric (Twaron) glued onto the strip foil layer, Kapton tape wrapped on the Twaron layer before glue curing phase, top and bottom flanges and angular bars applied.

Prior to exposing the prototype at DESY, an extensive characterization of the field cage has been done at CERN. The properties were extremely good concerning fiberglass flanges smoothness quality, gas tightness (measured leakage below 0.1 l/h), inner surface quality and deformations smaller than 0.2mm, compatible with prototype mold tolerances. We also performed several measurements of resistance and capacitance on the field and mirror strips showing the electric field is behaving as expected.

2.2. ERAM detector

An extensive description of the ERAM technology and of the detector used for the HA-TPCs of T2K is given in [6]. The ERAM modules built for T2K have a size of 420×340 mm^2 and are segmented in 32×36 rectangular pads of size 10.09×11.18 mm^2.

The ERAM are used to readout the ionization electrons produced by charged particles crossing the TPC gas volume. These electrons are drifted to the anode readout plane of the TPC under a uniform electric field. On the readout plane, an avalanche is generated by a high electric field in the ERAM amplification region and the 3D position of the track is reconstructed.

The main difference between the bulk-Micromegas, used for the existing ND280 TPCs, and an ERAM is that, in the case of bulk-Micromegas, the avalanche is smaller compared to the pad size for small drift distances, and therefore the position resolution is limited by the pad size. In the ERAM detectors, instead, the anode is covered by a foil of insulating material with a thin resistive layer on the top, spreading the charge over several pads. This allow for a better reconstruction of the track position.

The ERAM detector uses a Diamond-Like Carbon (DLC) thin layer sputtered on a 50 µm thick APICAL (Kapton) insulator sheet. The detector installed on the field cage, named ERAM-01, has a resistivity of 300–400 kOhm/□ using DLC foils stack on a 150 µm glue layer.

2.3. HA-TPC electronics

The full electronics chain that will be used for the HA-TPCs has been installed on the field cage prototype and tested during the test beam described in this paper.

The HA-TPC electronics is based on the use of the AFTER chips [7], that had been designed for the existing ND280 TPCs. The AFTER chip is a 72-channel device that includes preamplifiers and shapers with programmable gain and shaping time coupled to a 511-time bucket switched capacitor array

(SCA). During the test beam the electronics shaping time was set to 200 or 412 ns.

The Front-End Cards (FEC) have been newly designed and host 8 AFTER chips. They are installed parallel to the ERAM modules and two FECs are used to readout one ERAM (1152 channels). The response linearity of the FEC has been measured with a dedicated campaign and showed a uniform response of all the channels with typical deviations between neighboring pads not larger than 2%.

The two FECs on each ERAM are connected to a Front-End Mezzanine (FEM) card that performs the control, synchronization and data aggregation of the two FECs of a detector module.

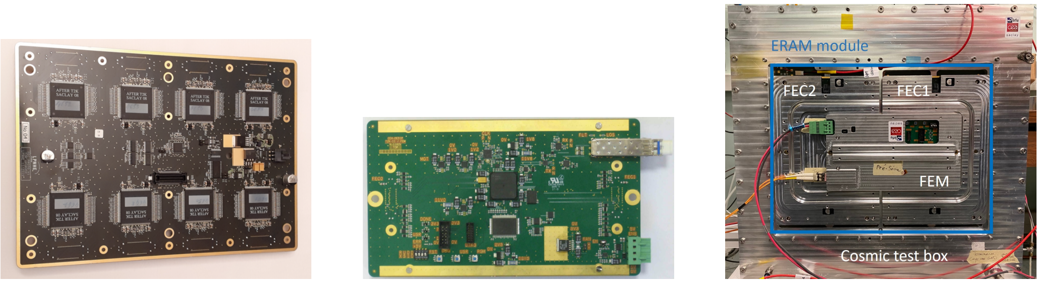

Figure 2: Photo of one FEC with the 8 AFTER chips (left), and of one FEM (center). On the right plot the two FECs are connected to the ERAM module and the FEM is connected on top of both FEC for signal readout.

As back-end electronics we used the TDCM, a generic clock, trigger distributor and data aggregator module designed for several projects, including the HA-TPCs.

3. Simulation of the ERAM response

In this paper we will present, for the first time, comparisons between the data and a Monte Carlo simulation of the ERAM detector. To develop the simulation we benefited from the already extensively verified simulation of the existing TPCs in the ND280. The new feature that was implemented in the model for this work is the resistive layer feature of the ERAM.

3.1. Simulation framework

The simulation starts from GEANT4 [8] that takes care of simulating the propagation of the charged particles in the TPC gas. To evaluate the energy loss and the produced ionization the PAI model [9] is used with at most a 1 mm computation step. The gas composition is the standard T2K gas [10], a mixture of Ar:CF_4:iC_8H_{10} (95:3:2).

The primary energy deposition by the charged particle is converted into the electron cloud. The ionisation potential for T2K gas is set to 26.8 eV. The electron cloud is later propagated to the ERAM plane. The arrival time is estimated based on the drift velocity. The electrons are spread following a Gaussian distribution on the sensitive plane assuming a transversal diffusion of $\sigma_{trans} = 0.29\ mm/\sqrt{cm}$ and a longitudinal diffusion of $\sigma_{long} = 0.21\ mm/\sqrt{cm}$.

For each electron arriving to the ERAM the amplification is simulated based on the ERAM gain G with the fluctuations estimated with exponential distribution as $gain = -log\,(1 - uniform(0, 1)) * G$.

The amplified signal is later spread on the resistive layer with the newly developed model that will be introduced in the next section. The resulting signal in each pad is then convoluted with the AFTER electronics response function and digitized with a sampling time of 40 ns.

3.2. Resistive layer simulation.

The behavior of the resistive layer can be approximated to the RC network [11]. In this model the charge density caused by the point-like signal is described with the solution of the diffusion equation

$$\rho_{charge}(t) = \frac{e^{\frac{r^2 RC}{4t}} RC}{2t} \tag{1}$$

where r is a distance from the initial charge deposition, t is time and RC is a network characteristic. To compute the observed charge in the pad the equation above should be integrated over the pad borders

$$\begin{gathered} Q_{pad}(t) = \int \int_{xy} \rho(t) \frac{1}{2} \pi \left(Erf\left[\frac{\sqrt{RC}x_1}{2\sqrt{t}}\right] - Erf\left[\frac{\sqrt{RC}x_2}{2\sqrt{t}}\right]\right) \\ \left(Erf\left[\frac{\sqrt{RC}y_1}{2\sqrt{t}}\right] - Erf\left[\frac{\sqrt{RC}y_2}{2\sqrt{t}}\right]\right) \end{gathered} \tag{2}$$

where Erf is an error function and $x_1,\ x_2,\ y_1,\ y_2$ are pad coordinates with respect to initial charge deposition.

The evolution of the charge in the pad is convoluted with the derivative of the electronics response:

$$E(t) = \frac{e^{-\frac{3\tau}{t_{peaking}}} \tau^3 \sin \frac{\tau}{t_{peaking}}}{t^3_{peaking}} \tag{3}$$

leading to the observable waveform (WF):

$$WF(t) = Q(t) \circledast \frac{dE}{dt}(t) \tag{4}$$

The numerical evaluation of the diffusion equation solution and of the convolution are extremely heavy in terms of computation time. To keep the simulation to a reasonable time several optimisations were included.

The first method is related to reducing the total number of avalanches to be simulated. The pad is divided into several smaller regions e.g. 3x3 or 5x5. All the avalanches that are detected in the same pad sub-region are merged into one and the charge is computed for the sum of all the contributions.

The next and the most significant optimisation is related to the pre-computation of the diffusion equation solution and convolution. Before starting the simulation the detector response is pre-computed for a unit charge, a given RC that is input to the model, and for all the positions across a x and y grid in the pad ($Q_{unit}(RC, x, y)$. The step of the grid can be tuned and for this work we divided the pad in a grid of 10×10. The obtained distributions are convoluted with the derivative of the electronics response to get the waveform (WF) for a unit charge. The final WF can be easily obtained by scaling the pre-computed solution with the charge obtained from GEANT4 $WF(t) = Q \times WF_{unit}(RC, x, y)(t)$. Thus there are no numerical computations during the simulation.

Two examples of the resulting WF, one for the data and one for the simulation, are shown in Fig. 3 for the leading and for two neighboring pads.

The two optimization described above allow to reduce the computing time by more than two order of magnitudes without impacting the simulation output as can be seen in Fig. 4 were no differences are observed for the spatial resolution with and without the optimization.

4. Characterization of ERAM detector

Each ERAM detector is scanned immediately after the production on an X-ray test bench at CERN. The test bench consists into a chamber with a

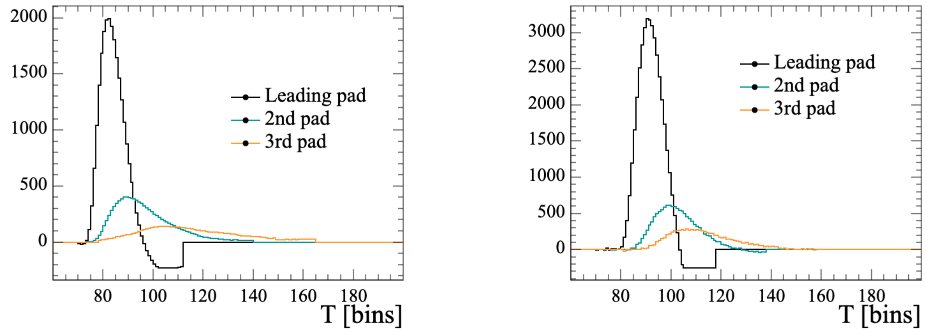

a b

Figure 3: The example waveforms for the leading and adjacent pads in (a) data and (b) MC.

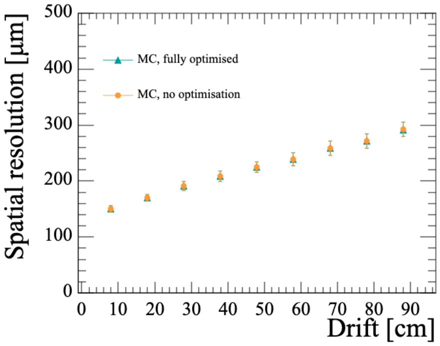

Figure 4: Spatial resolution for the MC simulation with and without optimisation.

3 cm width and is equipped with a robotic X-Y-Z arm system on an optical breadboard of 120×60 cm^2 holding a 250 Mbq ^{55}Fe source emitting 5.9 keV photons that deposit all their energy in the gas.

A 1.5 mm diameter collimation hole in front of the source assures that the majority of photo-electron arrives on the targeted pad. Prior to the scan, the ERAM is aligned to ensure the position of the source with respect to the center of each pad.

Each channel of the ERAM is scanned for $\sim$ 4 minutes at a rate of 100 Hz, allowing to reconstruct the spectrum of the ^{55}Fe source and compute the gain for each pad. An example of the ^{55}Fe spectrum for one pad is shown in Fig. 5.

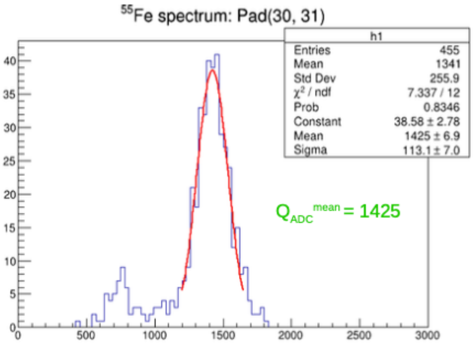

Figure 5: Measurement of the gain for one pad in the ERAM-01 from the ^{55}Fe source to be updated

Here is a description from the work of Shivam. We should make sure that the equations used by Shivam are same as the ones described in the simulation or change the description accordingly
For a typical event occurring in the center of one pad, a signal is observed on the pad directly hit by the photoelectrons but also on the eight neighboring pads. The nine waveforms for each event are then fitted taking into account the charge spreading and the response of the electronics, described in Eqs. 2, 3 and 4.

The fit of the waveforms allows to extract a value of RC and a value of gain for each channel. The corresponding maps for ERAM-01 are shown in Fig. 6. An average RC value of 120 ns/mm^2 with a good uniformity at the level of 10% over the whole module is observed.

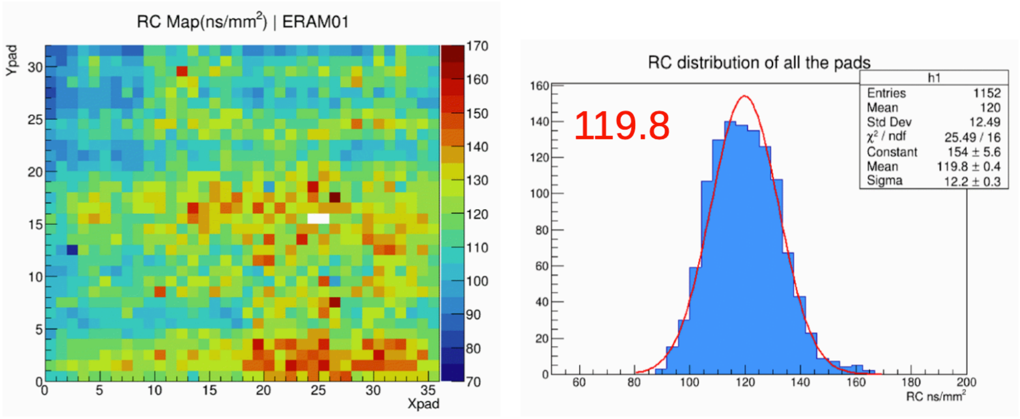

Figure 6: Measurement of RC for each pad of the ERAM-01 with the test bench data to be updated? Can we add also the gain map?

5. Collected Data at DESY

The High-Angle TPC prototype was filled with an Ar/CF_4/iC_4H_{10} (95/3/2) mixture, the same gas mixture that is used in T2K and was tested at DESY T24/1 facility. The chamber was placed inside the 1T PCMAG solenoid and exposed to the electron beam of 1 - 4 GeV/c momenta. The solenoid is equipped with a movable stage that allows moving the detector along the horizontal and vertical directions, and rotating ±45 degrees around a vertical axis. The TPC holder can be manually rotated inside the magnet.

The tests were aimed to ensure that the HA-TPC prototype design fully satisfies the requirement of the ND280 upgrade in particular focusing on testing the RC uniformity and charge spreading. Moreover, the drift distance range up to 1 m that corresponds to the maximum drift length of HA-TPC. Therefore, this test beam cover all the possible conditions of the final HA-TPC.

In order to test the setup parameters and configuration, various scans were performed. The gain scan was studied by varying the DLC voltage from 330 V to 380 V with the step of 10 V. Furthermore, the data were taken for two different drift velocities 78.7 and 58.7 $mm/\mu m$, where the former corresponds to T2K standard electric field E = 275 V/cm and the latter E=140 V/cm to the minimum transverse diffusion.

The PCMAG movable stage allows to perform drift distance and scans in X and Y. This is particularly interesting because non-uniformities in the RC, that are shown in Fig. 6 and that are due to the DLC foils, have been intentionally put on the Y direction. So during a scan in X the track will cross regions of the ERAM in which RC is uniform while in a scan in Y a track cross regions of the ERAM with different values of RC.

The drift distance scan was done for two values of the electronics shaping time of 412 ns and 200 ns.

The data were also collected for different rotation angles around the vertical and horizontal axis, within varying magnetic fields and for three drift distances, one close to the ERAM, one in the middle of the chamber, and one close to the cathode.

6. Reconstruction algorithms

Both, simulated and test beam tracks were reconstructed using the same analysis framework that uses DBSCAN [12] algorithm.

We select a track if it is crossing the whole detector without breaks or splits. A split is defined as the case where there is more than one cluster in a given column. An event containing a split is considered as a multiple track candidate and is rejected in our analysis. However, due to the large multiplicity (number of pads per cluster) induced by the resistive spreading, two close parallel tracks may not be separated by a gap and thus mis-reconstructed as one single track.

To reject such a topology and also to remove hairy and double tracks, a cut on the mean number of pad per cluster (multiplicity) of the track is applied. This cut depends on the track clustering algorithm that is used to reconstruct the tracks. As it was introduced in [6], we use horizontal and vertical clustering for tracks with incident angles below 30 degrees and above 70 degrees respectively, while for inclined tracks we use a diagonal clustering algorithm in which pads are combined into clusters according to their diagonal.

The mean multiplicity depends on the reconstruction algorithm and on the peaking time for the electronics. The mean multiplicity for horizontal and inclined tracks at small and large drift distance is shown in Fig. 7. As expected, for large drift distances, the multiplicity tend to increase due to the transverse diffusion of the electrons while crossing the gas volume. For the analysis presented in this paper we select tracks with mean multiplicity smaller than 3.4 for horizontal tracks and 2.2 for diagonal tracks with 200 ns peaking time.

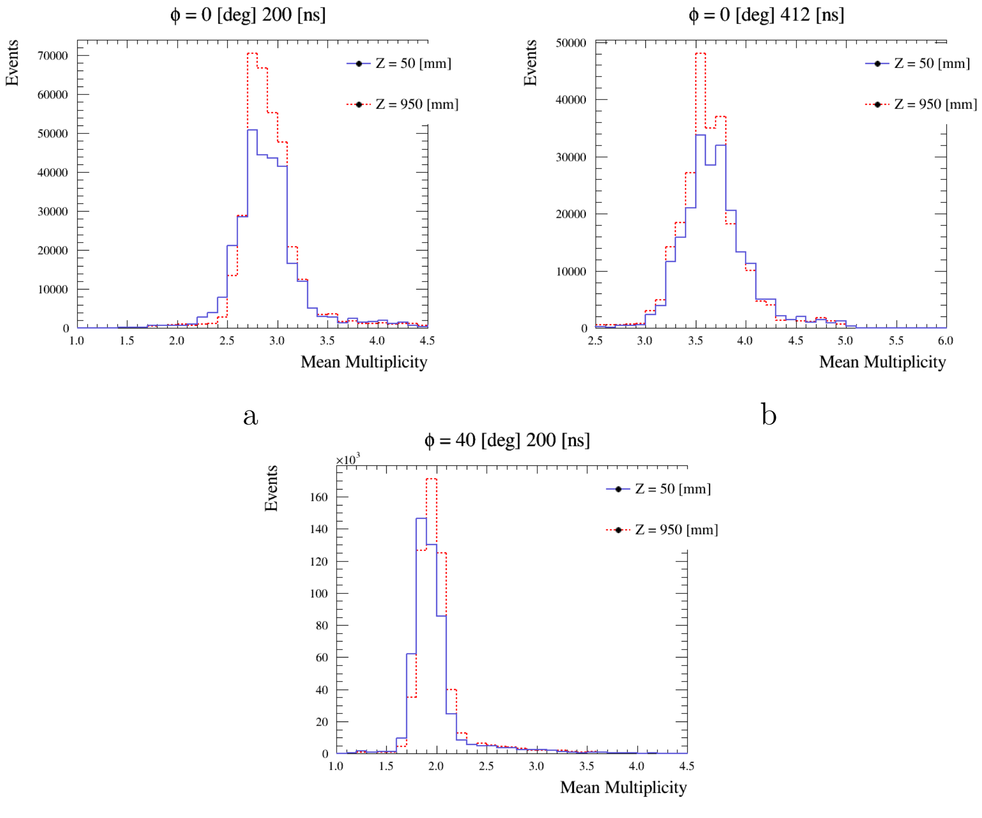

a b

c

Figure 7: Mean multiplicity at different peaking time for (a,b) horizontal and (c) inclined tracks at small and large drift distances.fix Z in the legend and add also the plot for 412 ns peaking time?

Finally, to compare with previous tests, the pads at the border are excluded from the reconstruction and hence horizontal tracks have 34 clusters while vertical tracks have 30.

7. Charge spreading characterization in data and simulation

To validate the newly introduced simulation, described in Sect.3, we produced horizontal electrons and we compare some some low-level variables including charge sharing and time differences, between data and simulation. These comparisons are done also with respect to the data taken at DESY in 2019 with a different ERAM module that is described in [6]. The comparison between data and simulation for spatial resolution and dE/dx resolution will be shown in Sect. 10.

For the low-level variables, the most significant for the resistive features characterisation are the charge ratio and the time difference between the WFs observed in the adjacent pad and the ones in the leading pad. These distributions are shown in Figs. 8 and 9.

For these comparisons, the charge in the pad is defined as the maximum of the waveform and the time is defined as the time bin at which the waveform was maximum. Since these variables depend a lot on the relative position of the track and the pad we sampled the distributions based on the reconstructed track position. This is less precise than using the true track position, but the only way that allows comparison with the data. For this study we use tracks close to ERAM plane to minimize possible effects induced by long drift.

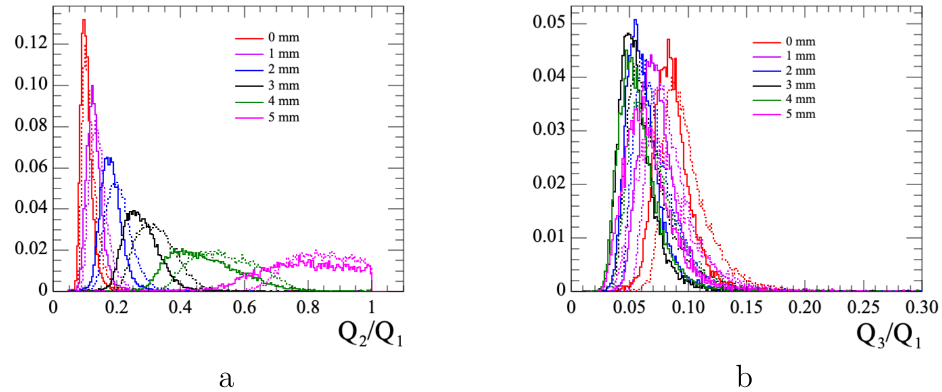

a

b

Figure 8: The distributions of the ratio of the second pad (a) and third pad (b) charge to the leading pad one sampled in the reconstruction track position with respect to the leading pad centre (color). The solid lines represent data and the dashed ones MC.

In order to make a quantitative comparison between data and Monte Carlo the distributions of Figs. 8 and 9 were fit with the Landau function and the MPV is plotted in 10 for these data (DESY 2021), the one from the previous test beam (DESY 2019) and MC samples generated with with RC=55 ns/mm^2 and RC=100 ns/mm^2.

The comparison clearly shows the different behaviour of the two ERAM modules. The difference can be explained by a different value of RC between the two modules. The data from 2021 are better reproduced by using

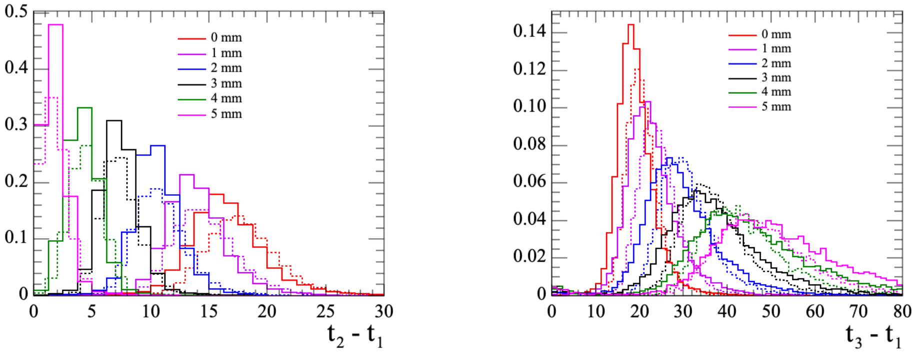

a b

Figure 9: The distributions of the time delay between the second pad (a), third pad (b) and the leading one sampled in the reconstruction track position with respect to the leading pad centre (color). The solid lines represent data and the dashed ones MC.

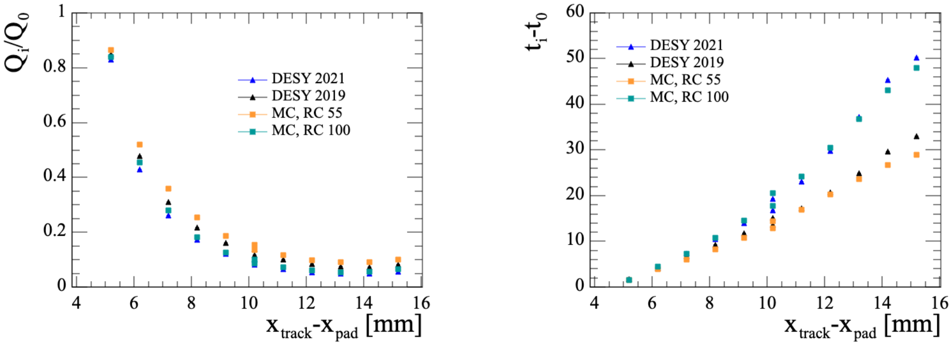

a b

Figure 10: The comparison of the low-level variables for the MC simulation and two testbeams 2021 and 2019: charge ratio (a) and time delay (b) between leading and adjacent pads versus the difference between pad centre and reconstructed track position.

RC=100 ns/mm^2 in reasonable agreement with the RC value measured with the test bench shown in Fig. 6.

8. Spatial resolution

The ND280 TPCs measure the momenta of the outgoing particles from neutrino interactions allowing to reconstruct the energy of the incoming neutrino, one of the critical element to precisely measure neutrino oscillations parameters.

The TPC momentum resolution depends on the spatial resolution [13] that can be precisely characterized with test beam data. For this analysis, the spatial resolution is measured by employing a "pad response function" (PRF) in the same manner as in [5, 6].

The distribution of the residuals in each cluster is fitted with a Gaussian and its width represents the spatial resolution. Each residual is the difference between the position of the track reconstructed locally (e.g. in one column) and the global fit. The track position measurement is performed with an iterative procedure. For the first step, all the tracks are reconstructed using the charge barycentric method. Such a method estimates the position of the track in a certain cluster by weighting the centre of the pad position by the charge in this pad. The estimated primary track positions in each cluster are then fit with a parabola over the whole detector (global fit). Based on the results of the fit, a pad response function scatter plot is filled for each pad. PRF function is defined as:

$$PRF(x_{track} - x_{pad}) = Q_{pad}/Q_{cluster} \tag{5}$$

where x_{track} and x_{pad} are positions of the track from the global fit and the center of the pad respectively and Q_{pad} and $Q_{cluster}$ are charges collected by the pad and by the whole cluster.

The PRF scatter plot is fitted with a ratio of two polynomes (the same as in [6, 14]). The scatter plot and the parametrization of the PRF are done independently for samples at different drift distances and inclination. The estimated parameters of the PRF analytical function are used further in the χ^2 minimization procedure to estimate the track position in each cluster.

$$\chi^2 = \sum_{pads} \left(\frac{Q_{pad}/Q_{cluster} - PRF(x_{track} - x_{pad})}{\sigma_{Q_{pad}/Q_{cluster}}} \right)^2 \tag{6}$$

where $\sigma_{Q_{pad}/Q_{cluster}} = \sqrt{Q_{pad}/Q_{cluster}}$.

In the following iterations the track position was evaluated from the fit. The iteration procedure is repeated while the spatial resolution keeps improving and it typically converges after three iterations. An example of PRF for horizontal and inclined tracks is shown in Fig. 11.

The spatial resolution was defined as a mean of the residual distribution for each cluster. An example for horizontal and inclined tracks is shown in Fig. 12. The distribution is expected to be center in zero and differences with respect to zero are the biases that will be discussed in Sect. 8.3.

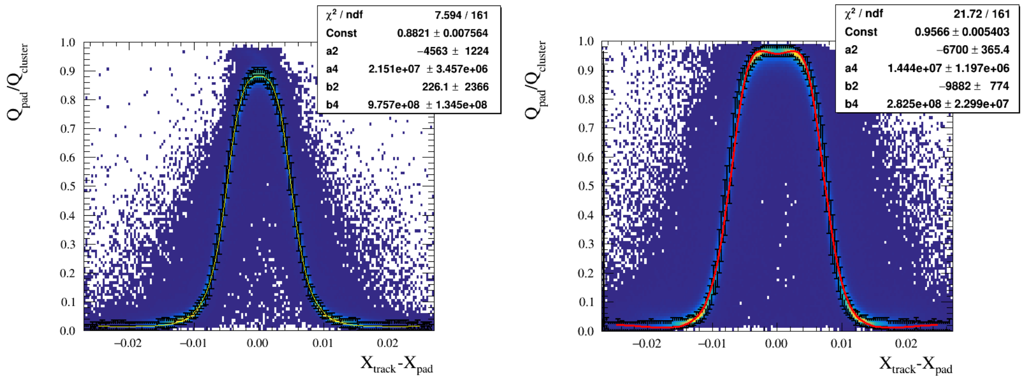

a

b

Figure 11: PRF function for (a) horizontal and (b) inclined tracks. add the units on X axis

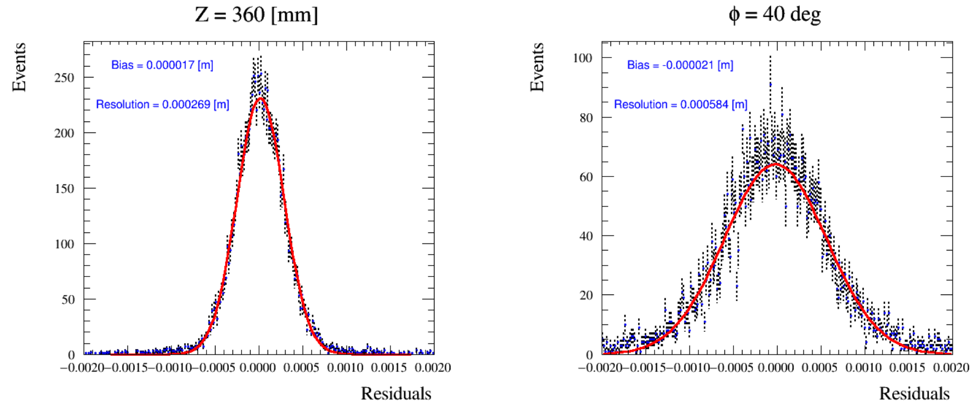

a

b

Figure 12: Residuals distribution for single cluster for (a) horizontal and (b) inclined tracks.add the units on X axis

8.1. Spatial resolution for horizontal tracks

With this method we can evaluate the spatial resolution for different topologies of track. The results for the horizontal tracks as a function of the drift distance for different electronics shaping time are presented in Fig. 13.

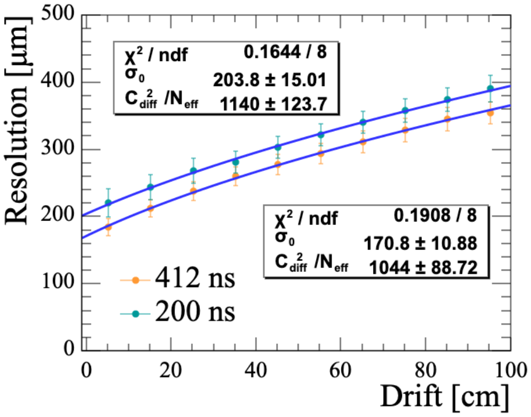

Figure 13: Spatial resolution with respect to the drift distance for the beam parallel to the pad side with a magnetic field of 0.2 T, drift velocity of 78.7 $mm/\mu s$ and peaking times of 200 ns and 412 ns.

The dependence of the resolution over the drift distance is expected to follow

$$\sigma = \sqrt{\sigma_0^2 + C_{diff}^2/N_{eff}} \tag{7}$$

where σ_0 is a resolution at 0 distance, C_{diff} is a transversal diffusion constant and N_{eff} is a number of effective electrons [15]. The observed dependence is in perfect agreement with this law. As expected, the peaking time doesn't affect C_{diff}^2/N_{eff} term, but changes the σ_0. A larger peaking time results in a higher amplitude in the neighbour pads. Thus we have more robust information for the PRF fit and the track position reconstruction is more precise.

The spatial resolution can also depend on the ERAM module characteristics, such as its gain and the local RC value. To check for these possible dependencies we used a scan done at fixed drift distance but with horizontal tracks crossing the ERAM at different X positions and vertical tracks crossing the ERAM at different Y positions. The spatial resolution obtained for the different X and Y position is shown in Fig. 14. No large differences are observed indicating that local non-uniformities on the ERAM module do not play a dominant role in the detector performances.

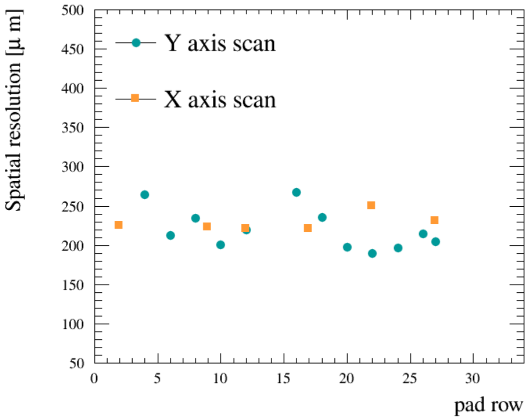

Figure 14: Spatial resolution versus different Y and X position at 412 ns peaking time.

8.2. *Spatial resolution for inclined tracks*

The collected test beam data allows studying spatial resolution as a function of the angle of inclination of the tracks within the ERAM module plane. The novelty with respect to the studies performed in [6] is that we could evaluate the spatial resolution performances for inclined tracks at long drift distances. The results are presented in Fig. 15, where angles from 0 to 30 degrees and from 70 to 90 clusters are defined perpendicular to the track direction (horizontal/vertical fit), and for the highly inclined tracks, with the angle between 40 and 60 degrees, the clusters defined along the diagonals as described in the section 6. In [6] it has been shown that the use of a diagonal fit for highly inclined tracks significantly improves the spatial resolution with respect to the use of horizontal or vertical fits.

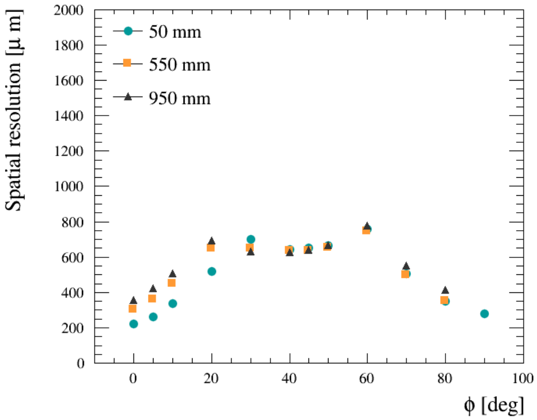

Figure 15: Spatial resolution versus different angles of the electron tracks inclination in the pad plane with 200 ns peaking time, 0.2T magnetic field and for various drift distances: 50 mm, 550 mm, 950 mm.

Fig. 15 demonstrates that, while the spatial resolution depends on the angle, it stays between 200 and 800 μm for all the analyzed samples. In particular, it is interesting to notice that, while the spatial resolution degrades with the drift distance for horizontal tracks, it is constant for inclined tracks.

The spatial resolution depends on the number of measurements (clusters) and a charge spread over a tolerable amount of pads (multiplicity). Therefore, a diagonal clustering algorithm has a twofold influence on spatial resolution measurements. On one side, it increases the number of clusters, on the other hand, leads to a smaller mean multiplicity than in the case of horizontal/vertical fit. With the diagonal fit pad size becomes effectively $\sqrt{2}$ times larger, thus degrading the spatial resolution but also making the effect of the transverse diffusion less significant.

Moreover, diagonal fit implies a dependence of the resolution on the track's length per pad. This cause an oscillatory behavior in the spatial resolution versus the cluster(Fig. 16 a). Fig. 16 b shows spatial resolution dependence on the track length per cluster for the tracks with 45 degrees angle of inclination. It is clearly seen that resolution linearly improves for longer segments in the pads.

8.3. Biases in spatial resolution

The bias of the track position in each cluster of the ERAM pad plane is defined as the mean of the gaussian of the distribution of residuals per

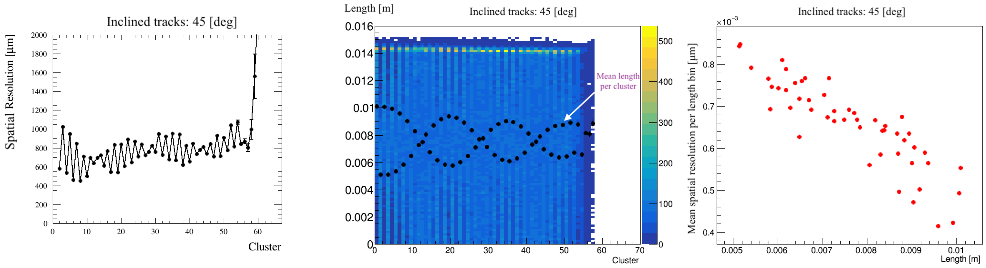

a b c

Figure 16: Tracks of 45 degrees inclination: spatial resolution per cluster (a), track length per cluster (b), mean track length with respect to spatial resolution (c).

cluster, and can be referred to as the systematic uncertainty of the track position estimation. In [6, 16] it is shown that the biases depends on the track position .The data collected during this campaign allow a deeper study of biases, in particular their dependence on drift distance for both horizontal and inclined tracks, as well as their behavior in various magnetic fields.

The bias per sample is defined as the arithmetic mean of the biases of all clusters. Fig. 17a shows the ratio between the bias and the spatial resolution as function of the drift distance for horizontal tracks. It is observed that biases are larger at short and long drift distances than at distances corresponding to the middle of the drift volume.

Similar behavior of the biases was observed for the inclined tracks (Fig. 17b). The tracks with the small angle (up to 30 degrees) were treated as horizontal tracks and reconstructed using the horizontal fit while the one with large angle (above 70 degrees) were reconstructed with vertical clustering. The ones at intermediate angles were reconstructed with the diagonal clustering.

It can be observed that for horizontal or vertical tracks, the biases degrade linearly with respect to the phi angle for the smallest and largest drift distances. For tracks reconstructed using diagonal clustering biases do not show a strong dependence on drift distances.

The dependence of the bias per column on the drift distance is shown in Fig. 18. For the smallest and largest drift distances, biases have visible patterns with large and opposite biases at the begin and at the end of the track. This patter is not observed for tracks in the center of the ERAM.

It was also noticed that biases disappear when the magnetic field is off. At 0 T biases depend on the drift distance linearly. The linear dependence is expected, since for larger drift distances the contribution to charge spread

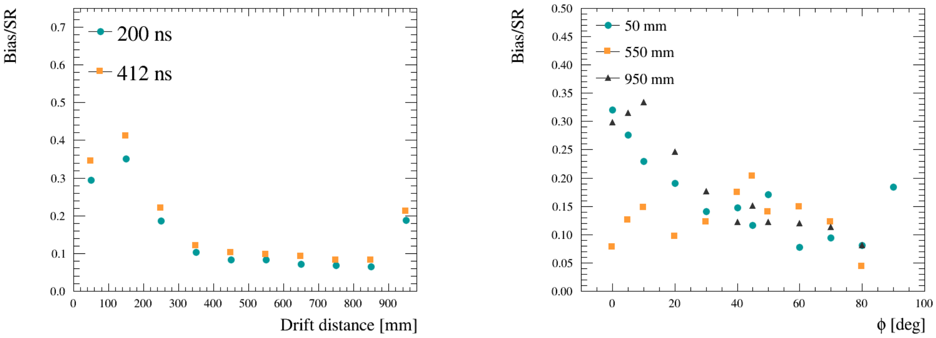

a b

Figure 17: Track position bias to spatial resolution ratio with respect to the drift distance for the beam parallel (a) and inclined (b) to the pad side with a magnetic field of 0.2 T, drift velocity of 78.7 $mm/\mu s$ and peaking times of 200 ns.

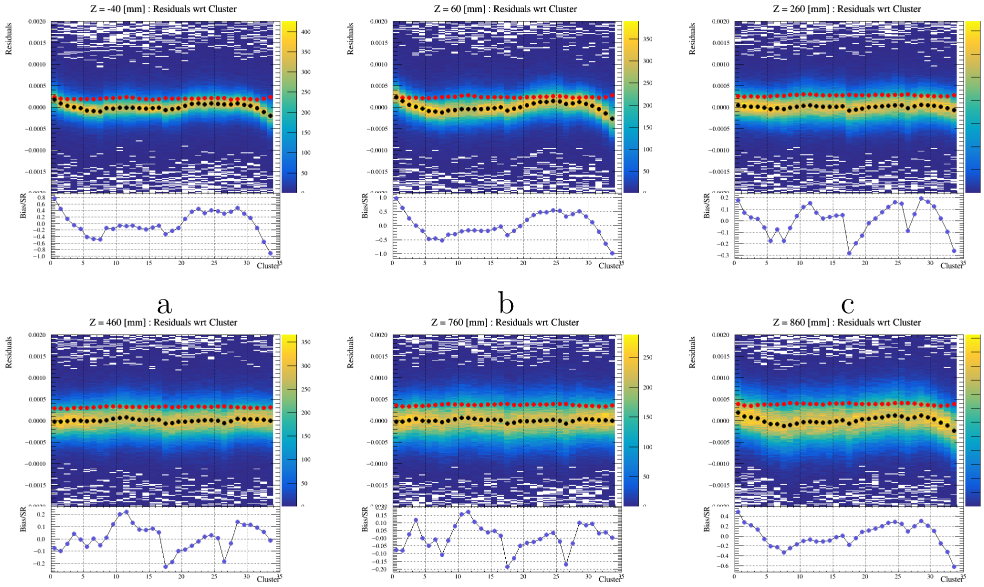

a b c

d e f

Figure 18: Spatial resolution, track position bias and their ratio distributions per cluster the beam parallel to the pad side with a magnetic field of 0.2 T, drift velocity of 78.7 $mm/\mu s$ and peaking times of 200 ns at various drift positions (z axis): -40 cm (a), 60 cm (b), 260 cm (c), 460 (d), 760 (e) and 860 cm (f).

of longitudinal diffusion is bigger which leads to an increase of PRF function width. However, under conditions when the magnetic field is on, the linearity is broken and distortions are observed (Figure 19) for short and long drift distances.

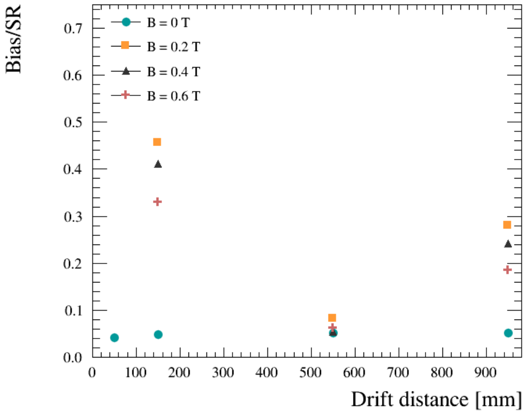

Figure 19: Track position bias to spatial resolution ratio with respect to the drift distance for the beam parallel to the pad side for different magnetic fields with drift velocity of 78.7 $mm/\mu s$ and peaking times of 200 ns.

To summarize, all the observed dependencies can point to the more complicated cause of biases such as combined contribution of inner detector non-homogeneities (resistive foil non-uniformity, gap size etc.) and magnetic field imperfection (ExB effect), and should be studied and accounted on using simulation. In general the ratio between the biases and the spatial resolution is smaller than 20% and the size of the biases is negligible for highly inclined tracks.

9. Deposited energy resolution

The other main goal of the HA-TPC will be to perform particle identification by measuring the deposited energy by charged particles crossing the gas. The TPC separation power will depend on the dE/dx resolution that can be evaluated with the data from this test beam.

In the context of T2K it is particularly important to be able to distinguish electrons and muons. Such an effort is crucial to estimate electron neutrinos contamination in the muon neutrino spectra and predict the un-oscillated amount of the electron neutrino in the far detector. To distinguish electrons and muons the deposited energy resolution requires to be better than 10 % to achieve a more than 3σ separation between electrons and muons.

The deposited energy is calculated per track using the truncated mean method already introduced in [6].

The method consists in calculating the track mean deposited energy by summing the deposited energy in the reduced number of clusters fired by the electron and ignoring the fraction of those that have a large energy contribution. Such contribution is caused by fluctuations in the ionization processes and leads to the smearing of the energy spectrum. The truncated mean method intended to refine the Gaussian form of deposited energy distribution, therefore, improving the energy resolution.

The truncation factor is optimized with the data and we found it to be 0.7 which is the same as for DESY test beam data of 2019 [6]. This means that 70% of the clusters are kept for deposited energy calculations.

The deposited energy per cluster was calculated by taking the maximum of the sum of the waveforms of the pads constituting the cluster. Various charge cluster definitions were studied in [6] and it was shown that the charge defined using the sum of the waveforms does not suffer from the pad signal double-counting effect resulting in a better deposited energy resolution.

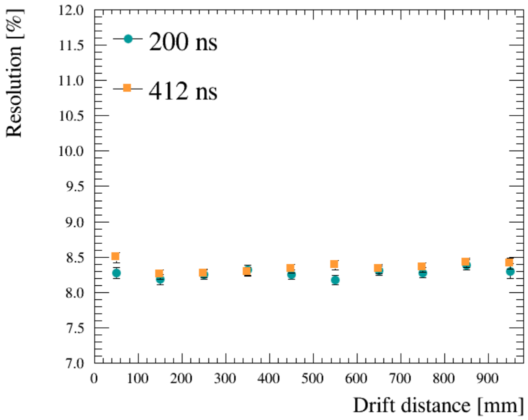

Figure 20: dE/dx resolution with respect to the drift distance for the beam parallel to the pad side with a magnetic field of 0.2 T, drift velocity of 78.7 $mm/\mu s$ and peaking times of 200 ns and 412 ns.

The deposited energy resolution was measured for both parallel and inclined tracks with respect to the pad side. Fig. 20 shows the deposited energy resolution measured for the parallel tracks for various drift distances.

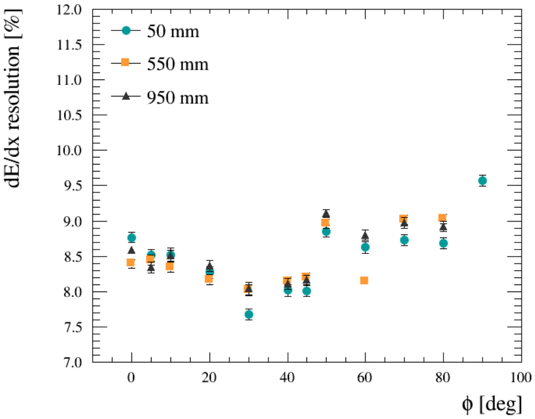

Figure 21: Deposited energy resolution versus different angles of the electron tracks inclination in the pad plane with 200 ns peaking time, 0.2T magnetic field and for various drift distances: 50 mm, 550 mm, 950 mm.

Fig. 21 shows the dE/dx resolution at various drift distances as a function of the angle within the pad plane. The tracks with the angles of inclination higher than 20 degrees and smaller than 70 degrees were reconstructed using the diagonal clustering.

Additionally, the deposited energy in tracks reconstructed with the diagonal fit were corrected on the track length in each cluster. Such correction accounts for the non-linear dependence of the charge with respect to the track length caused by the charge contribution from the neighbouring clusters for short track cluster length.

The study shows that dE/dx resolution is ∼8% for horizontal tracks and stays between 7.5 % and 9.6% for inclined and vertical tracks. Furthermore, it is independent of drift distance and on the electronics peaking time. It has been observed that dE/dx resolution is controlled by balancing two factors: the mean charge per cluster and the number of clusters. Fig. 21 shows that dE/dx resolution worsens for the angles $>$ 45 degrees since for such angles a smaller amount of clusters is reconstructed per track due to the rectangular shape of the ERAM.

Finally, as in the case of the spatial resolution, we looked for effects due to non-uniformities of the ERAM by using the X and Y scans. Results are show in Fig. 22.

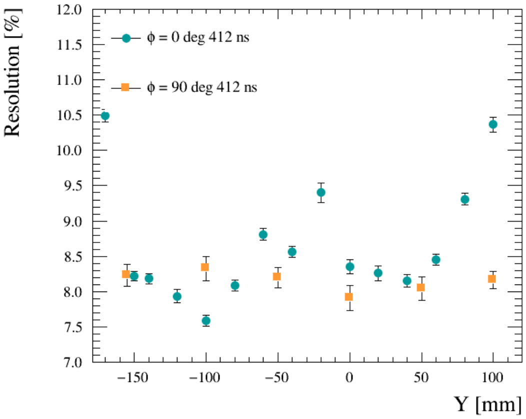

Figure 22: dE/dx resolution for tracks entering the ERAM at different X and Y positions.

The observed results prove that ERAM energy resolution capability corresponds to the requirements of the ND280 upgrade.

10. Comparison between data and simulation

In this section we compare the performances of the ERAM for spatial and dE/dx resolution between data and simulation.

Fig. 23 shows the spatial resolution for the data and MC samples as a function of the drift distance. The dependence over the drift distance was found to be slightly different using the nominal T2K value for the transversal diffusion ($\sigma_{trans} = 286\ \mu m/\sqrt{cm}$). The diffusion can be affected by the magnetic field configuration that is different from the T2K one.

We assume it to be a free parameter and tune the σ_{trans} in the model to reproduce the data better. A satisfactory agreement was found by increasing the transverse diffusion by 7%, changing it to $\sigma_{trans} = 310\ \mu m/\sqrt{cm}$.

In Fig. 24 we show the comparison in the spatial resolution between data and simulation for tracks at different angles. For completeness we make the comparison using both, 2019 and 2021 data. It should be noticed that the ϕ scan was done using different electronics peaking times and we did

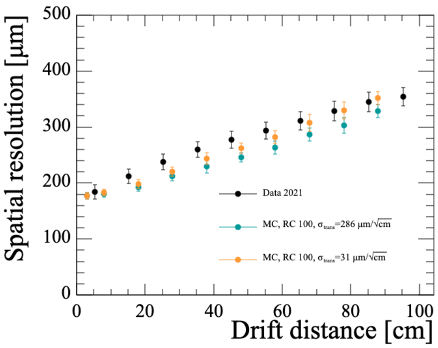

Figure 23: Spatial resolution over the drift distance for data samples from 2019 and 2021 and MC samples with different values for transversal diffusion.

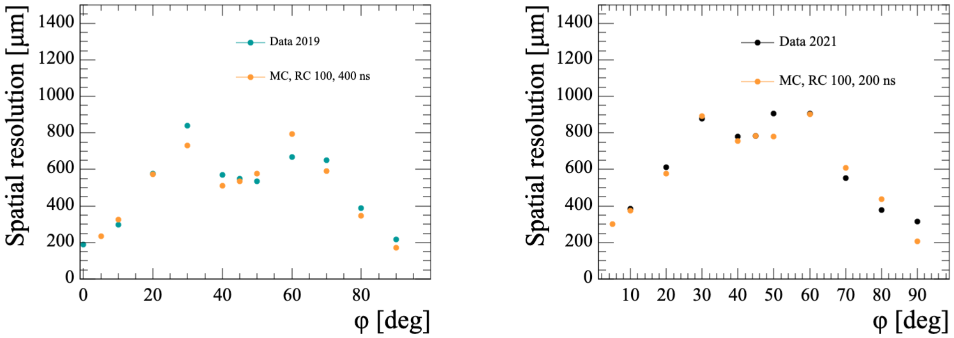

a

b

Figure 24: Spatial resolution over angle with respect to pad borders for data and MC samples. The data and MC samples uses (a) 400 ns and (b) 200 ns shaping time settings.

the simulation for the two cases. The simulation correctly reproduces the behaviour observed in the data.

Finally, in Fig. **??** it was found that the spatial resolution weakly depends on the drift distance for the highly inclined tracks. This effect was cross-checked and confirmed with the simulation. Fig. 25 shows large effect of the drift distance on the tracks close to 0° and 90°, but much smaller effect at 45°.

Finally, Fig. 26 shows the impact on the simulation of a different value of RC. The spatial resolution slightly degrades when RC increases but the effect is within $\sim 10\%$.

Concerning the deposited energy resolution, the simulation reproduces reasonably well the data for both, horizontal and inclined tracks as shown in

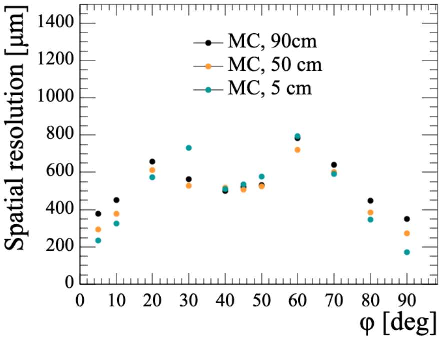

Figure 25: Spatial resolution as a function of the angle with respect to pad borders in the simulation for the different drift distances.

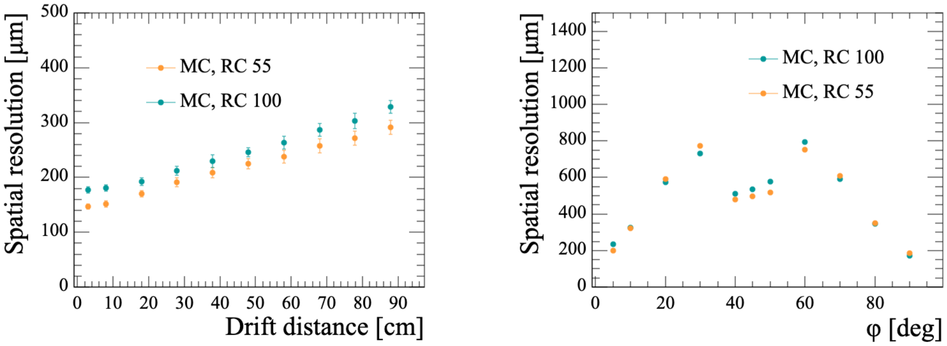

a

b

Figure 26: Spatial resolution versus drift distance and angles for simulations generated with different RC

Fig. 27.

11. Conclusions

We measured the performance of the ERAM prototype with beam particles at DESY. We studied both spatial and dE/dx resolution as a function of the angle of the track with respect to the ERAM plane. We also characterized charge spreading and produced a RC map of the prototype.

Spatial resolution better than 600 µm is obtained for all the angles using a dedicated clustering algorithm which is adapted to the track angle. Energy resolution better than 9% is obtained for all the angles. We expect ionization energy loss resolution to be better than 7% for tracks crossing two

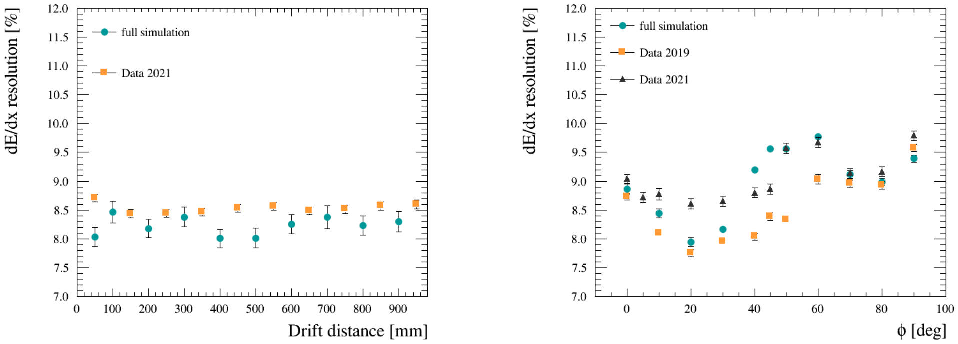

a b

Figure 27: dE/dx resolution for horizontal tracks as a function of the drift distance and for inclined tracks in DESY 2019 data, DESY 2021 data, and in the simulation.

ERAMs. Such performances fully satisfy the requirements for the upgrade of the ND280 TPC.

Acknowledgements

The measurements leading to these results have been performed at the Test Beam Facility at DESY Hamburg (Germany), a member of the Helmholtz Association. The authors would like to thank the technical team at the DESY II accelerator and test beam facility for the smooth operation of the test beam and the support during the test beam campaign.
We acknowledge the support of CEA and CNRS/IN2P3, France; DFG, Germany; INFN, Italy; National Science Centre (NCN) and Ministry of Science and Higher Education (Grant No. DIR/WK/2017/05), Poland; MINECO and ERDF funds, Spain.
In addition, participation of individual researchers and institutions has been further supported by H2020 Grant No. RISE-GA822070-JENNIFER2 2020, MSCA-COFUND-2016 No.754496, ANR-19-CE31-0001, RFBR grants #19-32-90100, the Ministry of Science and Higher Education of Russia (contract #075-15-2020-778) the Spanish Ministerio de Economía y Competitividad (SEIDI - MINECO) under Grants No. PID2019-107564GB-I00 and SEV-2016-0588. IFAE is partially funded by the CERCA program of the Generalitat de Catalunya.

References

[1] K. Abe, et al., The T2K Experiment, Nucl. Instrum. Meth. A659 (2011) 106–135. `arXiv:1106.1238`, `doi:10.1016/j.nima.2011.06.067`.

[2] K. Abe, et al., Observation of Electron Neutrino Appearance in a Muon Neutrino Beam, Phys. Rev. Lett. 112 (2014) 061802. `arXiv:1311.4750`, `doi:10.1103/PhysRevLett.112.061802`.

[3] K. Abe, et al., Constraint on the matter–antimatter symmetry-violating phase in neutrino oscillations, Nature 580 (7803) (2020) 339–344, [Erratum: Nature 583, E16 (2020)]. `arXiv:1910.03887`, `doi:10.1038/s41586-020-2177-0`.

[4] D. Attie, Beam tests of Micromegas LC-TPC large prototype, JINST 6 (2011) C01007. `doi:10.1088/1748-0221/6/01/C01007`.

[5] D. Attié, et al., Performances of a resistive Micromegas module for the Time Projection Chambers of the T2K Near Detector upgrade, Nucl. Instrum. Meth. A 957 (2020) 163286. `arXiv:1907.07060`, `doi:10.1016/j.nima.2019.163286`.

[6] D. Attié, et al., Characterization of resistive Micromegas detectors for the upgrade of the T2K Near Detector Time Projection Chambers, Nucl. Instrum. Meth. A 1025 (2022) 166109. `arXiv:2106.12634`, `doi:10.1016/j.nima.2021.166109`.

[7] P. Baron, D. Calvet, E. Delagnes, X. de la Broise, A. Delbart, F. Druillole, E. Monmarthe, E. Mazzucato, F. Pierre, M. Zito, AFTER, an ASIC for the readout of the large T2K time projection chambers, IEEE Trans. Nucl. Sci. 55 (2008) 1744–1752. `doi:10.1109/TNS.2008.924067`.

[8] S. Agostinelli, J. Allison, K. Amako, J. Apostolakis, H. Araujo, P. Arce, M. Asai, D. Axen, S. Banerjee, G. Barrand, F. Behner, L. Bellagamba, J. Boudreau, L. Broglia, A. Brunengo, H. Burkhardt, S. Chauvie, J. Chuma, R. Chytracek, G. Cooperman, G. Cosmo, P. Degtyarenko, A. Dell'Acqua, G. Depaola, D. Dietrich, R. Enami, A. Feliciello, C. Ferguson, H. Fesefeldt, G. Folger, F. Foppiano, A. Forti, S. Garelli, S. Giani, R. Giannitrapani, D. Gibin, J. J. G. Cadenas, I. González, G. G. Abril, G. Greeniaus, W. Greiner, V. Grichine, A. Grossheim,

S. Guatelli, P. Gumplinger, R. Hamatsu, K. Hashimoto, H. Hasui, A. Heikkinen, A. Howard, V. Ivanchenko, A. Johnson, F. W. Jones, J. Kallenbach, N. Kanaya, M. Kawabata, Y. Kawabata, M. Kawaguti, S. Kelner, P. Kent, A. Kimura, T. Kodama, R. Kokoulin, M. Kossov, H. Kurashige, E. Lamanna, T. Lampén, V. Lara, V. Lefebure, F. Lei, M. Liendl, W. Lockman, F. Longo, S. Magni, M. Maire, E. Medernach, K. Minamimoto, P. de Freitas, Y. Morita, K. Murakami, M. Nagamatu, R. Nartallo, P. Nieminen, T. Nishimura, K. Ohtsubo, M. Okamura, S. O'Neale, Y. Oohata, K. Paech, J. Perl, A. Pfeiffer, M. G. Pia, F. Ranjard, A. Rybin, S. Sadilov, E. D. Salvo, G. Santin, T. Sasaki, N. Savvas, Y. Sawada, S. Scherer, S. Sei, V. Sirotenko, D. Smith, N. Starkov, H. Stoecker, J. Sulkimo, M. Takahata, S. Tanaka, E. Tcherniaev, E. S. Tehrani, M. Tropeano, P. Truscott, H. Uno, L. Urban, P. Urban, M. Verderi, A. Walkden, W. Wander, H. Weber, J. P. Wellisch, T. Wenaus, D. C. Williams, D. Wright, T. Yamada, H. Yoshida, D. Zschiesche, Geant4 – a simulation toolkit, Nuclear Instruments and Methods in Physics Research Section A: Accelerators, Spectrometers, Detectors and Associated Equipment 506 (2003) 250–303. `doi:10.1016/S0168-9002(03)01368-8`.
URL `http://www.sciencedirect.com/science/article/pii/S0168900203013688%7B%5Ctextbackslash%7Dnhttp://linkinghub.elsevier.com/retrieve/pii/S0168900203013688`

[9] J. Apostolakis, S. Giani, L. Urban, M. Maire, A. V. Bagulya, V. M. Grichine, An implementation of ionisation energy loss in very thin absorbers for the geant4 simulation package, Nuclear Instruments and Methods in Physics Research Section A: Accelerators, Spectrometers, Detectors and Associated Equipment 453 (2000) 597–605. `doi:10.1016/S0168-9002(00)00457-5`.

[10] N. Abgrall, et al., Time Projection Chambers for the T2K Near Detectors, Nucl. Instrum. Meth. A637 (2011) 25–46. `arXiv:1012.0865`, `doi:10.1016/j.nima.2011.02.036`.

[11] M. S. Dixit, A. Rankin, Simulating the charge dispersion phenomena in micro pattern gas detectors with a resistive anode, Nucl. Instrum. Meth. A566 (2006) 281–285. `arXiv:physics/0605121`, `doi:10.1016/j.nima.2006.06.050`.

[12] M. Ester, H.-P. Kriegel, J. Sander, X. Xu, A density-based algorithm for discovering clusters in large spatial databases with noise, in: Proceedings of the Second International Conference on Knowledge Discovery and Data Mining, AAAI Press, 1996, pp. 226–231.

[13] R. Gluckstern, Uncertainties in track momentum and direction, due to multiple scattering and measurement errors, Nuclear Instruments and Methods 24 (1963) 381–389. `doi:https://doi.org/10.1016/0029-554X(63)90347-1`.
URL `https://www.sciencedirect.com/science/article/pii/0029554X63903471`

[14] K. Boudjemline, M. S. Dixit, J. P. Martin, K. Sachs, Spatial resolution of a GEM readout TPC using the charge dispersion signal, Nucl. Instrum. Meth. A574 (2007) 22–27. `arXiv:physics/0610232`, `doi:10.1016/j.nima.2007.01.017`.

[15] P. Colas, First test results from a Micromegas large TPC prototype, Nucl. Instrum. Meth. A623 (2010) 100–101. `doi:10.1016/j.nima.2010.02.161`.

[16] A. Bellerive, K. Boudjemline, R. Carnegie, M. Dixit, J. Miyamoto, E. Neuheimer, A. Rankin, E. Rollin, K. Sachs, J. P. Martin, V. Lepeltier, P. Colas, A. Giganon, I. Giomataris, Spatial resolution of a micromegas-tpc using the charge dispersion signal (2005). `doi:10.48550/ARXIV.PHYSICS/0510085`.
URL `https://arxiv.org/abs/physics/0510085`